Multi-thermals and high concentrations of secondary ice: A modelling study of convective clouds during the ICE-D campaign

Zhiqiang Cui[1], Alan Blyth[1,2], Gary Lloyd[3], Thomas Choularton[3], Keith Bower[3], Paul Field[1,4], Rachel Hawker[1], Lindsay Bennett[2]

5   [1]Institute for Climate and Atmospheric Science, University of Leeds, Leeds, LS2 9JT, UK
[2]National Centre for Atmospheric Science, Leeds, LS2 9PH, UK
[3]Centre for Atmospheric Science, University of Manchester, Manchester, M13 9PL, UK
[4]Met Office, Exeter, UK

10   *Correspondence to*: Zhiqiang Cui (z.cui@leeds.ac.uk)

Abstract. This paper examines the mechanisms responsible for the production of ice in convective clouds influenced by mineral dust. Observations were made in the Ice in Clouds Experiment – Dust (ICE-D) field campaign which took place in the vicinity of Cape Verde during August 2015. Measurements made with instruments on the FAAM aircraft through the clouds on 21 August showed that ice particles were observed in high concentrations at temperatures greater than about -8 °C.

15   Sensitivity studies were performed using existing parametrisation schemes in a cloud model to explore the impact of the freezing onset temperature, the efficiency of freezing, mineral dust as efficient ice nuclei, and multi-thermals on secondary ice production by the rime-splintering process.

The simulation with the default Morrison microphysics scheme (Morrison et al., 2005) that involved a single thermal

20   produced a concentration of secondary ice that was much lower than the observed value of total ice number concentration. Relaxing the onset temperature to a higher value, enhancing the freezing efficiency, or combinations of these, increased the secondary ice particle concentration, but not by a sufficient amount. Simulations that involved only dust particles as ice nucleating particles produced a lower concentration of secondary ice particles, since the freezing onset temperature is low. The simulations implicate that a higher concentration of ice nucleating particles with a higher freezing onset temperature

25   may explain some of the observed high concentrations of secondary ice. However, a simulation with two thermals that used the original Morrison scheme without enhancement or relaxation produced the greatest concentration of secondary ice particles. It did so because of the increased time that graupel particles were exposed to significant cloud liquid water content in the Hallett-Mossop temperature zone. The forward-facing camera and measurements of the vertical wind in repeated passes of the same cloud suggested that these tropical clouds contained multiple thermals. Hence, in a similar way to other

30   convective clouds observed elsewhere in the world, it is likely that multi-thermals play an important role in producing very high concentrations of secondary ice particles in some tropical clouds.

1 Introduction

Ice particles in clouds contribute to the formation of more than half of the world's precipitation and greatly enhance the amount of precipitation process over the warm rain only process (McFarquhar et al., 2017). Precipitation in deep convective clouds is closely related to the riming and melting of ice particles (Cui et al., 2011). Ice phase processes in clouds affect not only the weather but also the climate, which is a new frontier of research in terms of aerosol-cloud-climate interactions (Seinfeld et al., 2016; Storelvmo et al., 2017).

Cloud drops form on cloud condensation nuclei (CCN), and primary ice particles on ice nucleating particles (INPs). The main INP types include mineral and desert dust, metals and metal oxides, organics and glassy particles, bioaerosol, soil dust, biomass and fossil fuel combustion aerosol particles, volcanic ash particles, and crystalline salts (Kanji et al., 2017). The onset and median freezing temperatures of those INPs show great intra- and inter-type variabilities (Kanji et al., 2017). An upper limit of the starting freezing temperatures of some bacteria INPs is typically between -2 to -4 ºC (Szyrmer and Zawadzki, 1997; Morris et al., 2008), and some even as high as -1.5 ºC (Kim et al., 1987, Lindow et al., 1989). The activation temperature of mineral dust is less than -15 ºC (Hoose and Möhler, 2012), but depends on their minerology (Murray et al., 2012). However, dust particles can serve as INPs at higher temperatures if the fraction of potassium-rich feldspar (K-feldspar) is high because feldspar particles have high ice-nucleating active sites (Atkinson et al., 2013). A full functionalization of nucleating sites of a feldspar particle with hydroxyl groups enables a strong bonding to the prismatic plane of ice and prompts formation of ice crystals on the surface of the feldspar (Kiselev et al. 2017), which favours a higher freezing temperature. A recent study showed that a microcline mineral (a potassium-rich alkali feldspar) has bulk freezing temperatures even greater than -3 ºC (Kaufmann et al., 2016). It has also been found that sea-spray aerosol particles can serve as INPs (e.g., Wilson et al., 2015, DeMott et al., 2016), but they do not active until the temperatures fall below -14 ºC. Burrows et al. (2013) suggested strong regional differences in the importance of marine biogenic INP relative to dust INP.

Nickovic et al. (2012) developed a high-resolution global dataset of mineral composition and showed the effective mineral content in soil for quartz, illite, kaolinite, smectite, feldspar, calcite, hematite, gypsum and phosphorus. For example, the gradients of the surface content of feldspar is particularly strong in Central Sahara. What makes the INPs even more complex is that they can be chemically and physically modified through chemical processing, internal and/or external mixing, and cloud processing (Kanji et al., 2017).

Ice particles form via various primary pathways with the help of INPs, such as deposition ice nucleation, contact freezing, immersion freezing, condensation freezing, collisional contact freezing, and inside-out evaporation freezing (e.g., Cooper, 1986). Ice particles also form homogeneously at temperatures about -40 ºC. The INP concentrations are highly variable at a temperature. Most, if not all, models represent the widespread relationships with parameterization schemes. There is no one-size-fits-all solution to parameterize freezing processes for all INPs.

Apart from the primary freezing processes, new ice crystals can be produced by secondary ice production (SIP) in the presence of preexisting ice without INPs. There are several SIP processes: fragments emitted from freezing large drops (e.g., Wildeman et al., 2017), mechanical breakup of ice crystals by collision with other particles (e.g., Knight, 2012), splinter formation during the riming process (Hallett and Mossop, 1974), enhanced ice nucleation in regions of spuriously high

70 supersaturations (Hobbs and Rangno, 1990), ice particle fracture during evaporation of ice particles (Oraltay and Hallett, 1989; Bacon et al., 1998). Of those processes, the Hallett-Mossop parameterization has been studied the most and is routinely incorporated in models. New parameterizations for other mechanisms have been developed recently (e.g., Phillips et al., 2017; Lawson et al., 2017). Observational and modelling studies have shown that the observed high ice concentration in some clouds may be explained with the Hallett-Mossop process (e.g., Huang et al., 2008; Crosier et al., 2011; Crawford et

75 al., 2012; Huang et al., 2017; Hawker et al., 2021). For a complete review of the literature on the secondary ice production, including the current state and recommendations for the future research, see Field et al. (2017).

Numerical models, including cloud models, commonly do not explicitly include the information about CCN and INP, but rather use parameterizations to represent a "general" or a best-fit case for a freezing mode in the primary ice production. As a

80 result, a parameterized microphysics scheme does not reflect the aerosol environment of a cloud. Any departure of the INP properties from the best-fit condition, such as the onset freezing temperature and the freezing efficiency, may lead to an unrealistic representation of the cloud microphysics.

Ice production in clouds is affected not only by microphysical processes, but also by cloud dynamics. Previous studies have

85 revealed that thermals are the building blocks of convective clouds (Koenig, 1963; Blyth et al., 1988; Keller and Sax, 1981; Blyth et al., 2005; Damiani et al., 2006). The clouds often contained multiple thermals that ascended in the wake of their predecessors. In a theoretical study using a detailed microphysics model in a simple dynamical framework, Blyth and Latham (1997) found that multi-thermals can help yield rapid ice HM multiplication by providing a new source of liquid water content and by allowing the particles to be carried by the thermal circulation. The results were consistent with those

90 found earlier by Koenig (1963) and others.

The field campaign of ICE-D took place in the Cape Verde region, downwind of the African dust sources, in August 2015. It occurred before the recommendation was made by Field et al (2017) to 'carry out integrated field programs involving in-situ sampling, remote sensing, and modelling studies'. However, the analysis of data from the project are still ongoing and hence

95 addresses the recommendation. Although there have been previous field campaigns relevant to ice nucleation in and near the Saharan region, most of them focused on chemical and physical properties of the dust particles and their impact on large scale phenomena (e.g., Knippertz et al., 2011; Rocha-Lima et al., 2018). The ICE-D was specifically designed to study how dust affected ice production in convective clouds using aircraft measurements, radar, and ground-based aerosol instruments,

which was complementary to a series of projects of layer clouds (ICE-L, see Heymsfield et al., 2011) and tropical towering
100 clouds (ICE-T, see Heymsfield and Willis, 2014).

A suite of instruments on board the UK research aircraft FAAM BAe 146 measured the information about cloud
microphysics, aerosol particles, and other atmospheric variables (see Price et al., 2018, Liu et al., 2018, and Lloyd et al.,
2020 for further descriptions). Aircraft measurements were made on 21 August 2015 of convective clouds about 150 km
105 from the Praia airport, Cape Verde. There are two main points from the observations. Firstly, the maximum concentration of
ice particles was as greater than 200 per litre, greater than expected from INP alone. Secondly, the first ice particles appeared
at temperatures greater than -8 ℃.

In this paper, we report on a modelling study designed to explore several aspects of the production of ice particles. Namely:
110 the impact of the freezing onset temperature; the impact of the efficiency of freezing on secondary ice production in
microphysics schemes; to inspect the relationship between the measured dust as efficient INPs and the secondary ice
production; and to investigate the role of multi-thermals in producing high secondary ice concentrations. A three-dimensional
cloud model was used for the simulations. Section 2 describes the observations and datasets. The model description and
numerical designs is in Section 3. Section 4 presents the simulation results. The final section provides the summary and
115 conclusions.

2. Summary of the observations

The observations of the ICE-D field campaign involved in aircraft, radar and ground-based measurements. The UK's Facility
for Airborne Atmospheric Measurements (FAAM) BAe-146 research aircraft was used to conduct airborne measurements of
cloud microphysics and aerosol One airborne aerosol instrument was the Passive Cavity Aerosol Spectrometer Probe
120 (PCASP), which can measure both aerosol number and size in the nominal size range 0.1 to 3 micrometers. (Price et al.,
2018; Liu et al., 2018). Ice particle concentrations were derived from the 2D-S Stereo Probe, an optical imaging instrument
that obtains stereo cloud particle images and concentrations using linear array shadowing (Lawson et al., 2006; Cui et al.,
2012; Cui et al., 2014). The UK Met office ALS450 lidar manufactured by Leosphere with an emitted wavelength of 354.7
nm and a receiver bandwidth of 0.36 nm was on board the aircraft to measures cloud top height, range corrected signal,
125 relative depolarisation ratio so that to map cloud and aerosol layers, retrieval of aerosol optical properties (Marenco et al.,
2013). A mobile dual-polarisation Doppler X-band weather radar (Neely III, et al., 2018) of the National Centre of
Atmospheric Science, UK was deployed at the Praia airport on the island of Santiago, Cape Verde. A suite of instruments
was positioned at the airport to measurement aerosol properties (Marsden et al., 2019).

130 A trough existed along the west coast of Africa (Figure 1a) on 21 August 2015. Convective cloud systems and some smaller
and more isolated convective clouds developed along the coast.

The aircraft operated in the region from longitude 23.541° W to 21.022° W and from latitude 13.494° N to 15.024° N. The operation region was characterized by relatively low aerosol optical depth (AOD), compared with the dust-plume region between -20° W - -5° W and 18° N – 26° N (Figure 2a). The aerosol subtype image by CALIPSO overpass to the west of the

135   region indicates the existence of a dust layer (in yellow) about 2-km thick (Figure 2b). The aerosol below the dust layer was dominated by clean marine aerosol with some polluted dust. Images from the on-board Lidar show that the range-correlated Lidar signal, which is an indicator of aerosol loading, was much stronger below 1.5 km just after taking off. However, there was a layer with a slightly weaker signal at about 2.3 km during the profile in Figure 2c, which was approximately 150 km to the west of the clouds shown in Figure 1. The relative depolarization ratio (spheres close to 0 and non-spheres much higher)

140   indicates the aerosol particles were soluble below 1.5 km within the boundary layer and insoluble in the aloft layer (Figure 2d). The Lidar signals were consistent with the PCASP measurement in Fig. 1e, which also shows the two aerosol layers. Together with the CALIPSO image, we can conclude the aloft aerosol layer was mostly dust.

The aircraft penetrated clouds between 100 and 300 km to the southeast of Praia at various levels in the ambient temperature

145   range of -1 to -7 ºC. Only the outside-cloud temperatures were used to avoid the bias caused by wetting. The aircraft followed the ascending cloud top wherever possible and made the passes a few hundred metres below the top in order to detect the formation and production of primary and secondary ice particles.

Figure 2 shows the concentrations of ice particles of several passes from the aircraft measurements. The maximum

150   concentrations were 44 L^{-1} for a pass at -3.1 ºC (~5500 m), 52 L^{-1} at -4.4 ºC (~5800 m), 270 L^{-1} at -4.7 ºC (~6100 m), and 82 L^{-1} at -6,8 ºC (~6500 m). As an example, the time series of concentration and vertical velocity for the pass with the highest concentration is shown in Figure 3. Two points can be drawn based on the figure. Firstly, the ice particles appeared at temperatures greater than -10 ºC. Secondly, the ice concentrations were much higher than the predicted by the primary ice production. Therefore, secondary ice production definitely occurred in the clouds.

155   ## 3. Cloud Modelling

3.1 Model description

Cloud model 1 (CM1) is primarily designed for idealised simulation of convective clouds using relatively less memory which allows it to run quickly. CM1 uses conserved mass and energy conservation numerical schemes in 3-dimensions. The model has a rich choice of microphysics schemes. More details on the model can be found in Bryan et al. (2003) and Bryan

160   and Morrison (2012). In our simulations, the Morrison double-moment microphysics scheme (Morrison et al., 2005) was used to predict the mass ratio and the number concentration of cloud droplet, rain, ice, snow and graupel. The microphysical processes include drop activation, condensation, evaporation, collision and coalescence, primary freezing modes of deposition/condensation, contact, and immersion, and secondary freezing through the riming-splintering (the Hallett-Mossop) process, and the transition and interaction between different species.

3.2 Experimental design

165

One of the objectives is to investigate the impact of the onset freezing temperature and the freezing efficiency on the secondary ice production. As is discussed in the introduction, the onset temperatures vary with the type of the INPs. The Morrison scheme uses the Cooper parameterization (Cooper, 1986), in which freezing begins at a temperature of -8° C. Similarly, the temperature where freezing begins depends on the INP types. Recently, Garimella et al. (2018) summarised

170 some of the limitations of field measurements of INP and the influence on cloud simulations. The parameterizations derived from field and laboratory data using the continuous flow diffusion chambers (CFDCs) for example, are subject to systematic low biases due to the limit of detection, not experiencing the maximum supersaturation, and the concurrence of ice particles with drops. To reduce the bias, DeMott et al. (2015) proposed to apply a calibration factor of 3 to multiply the measured INP to obtain a better agreement. However, Garimella et al. (2017) noted that the factor was 4 using the Spectrometer for Ice

175 Nuclei, and it varied in the range from about 1 to 10, which indicates that this is one of the major problems in quantifying the formation of ice in numerical models.

As a result of this uncertainty, we investigate the influence of the onset temperature and the efficiency on the ice production in sensitivity simulations using the Morrison scheme as the control run. We also modify the Cooper parameterization in the

180 Morrison scheme with a parameterization of DeMott et al. (2010) based on all available data as a function of temperature. A recently-developed parameterization by Paukert and Hoose (2014) is also tested to probe whether dust INPs alone can produce the concentration of ice observed by the aircraft. The details of the control and the sensitivity model runs are given in Table 1. The aims of the sensitivity simulations are summarised as follows. RLX examined the effect of active INPs at higher temperatures on secondary ice production. TEN explored the effect of more INPs. RLXTEN combined effects of the

185 above two, while RLX3X100 and RLX2X100 probed the effect of even higher loadings of INPs. The DeMott scheme was examined in runs DMTA, DMTRLX, and DMTRLX2 and the effect of dust in PAUKERT and PAUKERTD. Finally, the effect of multi-thermals on secondary ice production was examined in THERMALS.

3.3 Model setup

190

The domain contains 100×100 grid points in the horizontal direction and 80 levels in the vertical direction, with a grid spacing of 150 m in the three directions. Most of the simulations had a duration of 60 min except for the multi-thermal and the Paukert-scheme runs which have a 120 min duration. The model was initialised with a horizontally homogeneous atmosphere. Initial profiles of potential temperature and water mixing ratio were taken from measurements made by

195 radiosondes released from the aircraft in the vicinity of the clouds studied. Because the release level of the dropsonde is lower than the highest level of the model domain, we used the NCEP/NCAR reanalysis data close to the cloud to represent the air above the radiosonde drop-off level. The simulated clouds were triggered by a warm bubble of 2 ºC in the control and most of the sensitivity runs except the multi-thermal run where another bubble was added 20 min from the starting time.

4. Results

4.1 Control simulation

Figure 4 shows a time sequence of a cross-section along the centre of the simulated cloud for the control run (CTL) with only one thermal. The cloud ascended generally at a rate of 300 m per minute between 20 and 25 min. The maximum vertical wind was 17.7 ms^{-1} at 20 min and 8.3 ms^{-1} at 25 min; thereafter, it ascended at a rate about 150 m per minute to 36 min. The maximum vertical wind was 6.4 ms^{-1} at 30 min and 4.4 ms^{-1} at 35 min. The maximum level of cloud top was 9075 m at 36 min. Figure 4a shows that there was a column of supercooled raindrops up to a temperature of about -5 °C (6.3 km). There were no ice crystals or graupel particles. The cloud top temperature was about -6 °C at the time. At 25 min, the cloud top reached about 8 km (T ~ -14 ºC). Ice particles were present in the upper 500 m with a maximum concentration of 0.5 L$^{-1,}$ but there were no graupel particles. The column of supercooled raindrops reached a temperature of about -14C. There are few, if any observations of such cold columns, especially in tropical oceanic clouds. At 30 min, the graupel particles fell down into the HM zone, presumably around the edges of the thermal in the downdrafts and then at the rear of the thermal where the updraft is much weaker. The arrival of the graupel in the HM temperature zone allowed for splinters to be produced by the HM process. The graupe and ice concentrations in the HM zone reached 0.35 L^{-1} and 4.1 L^{-1}, respectively. The cloud had further developed by 35 min such that the top had reached an altitude of about 9 km (T ~ -22 ºC); the maximum height. The concentrations of ice in the HM zone and at the cloud top were 2.1 L^{-1} and 14.5 L^{-1}, respectively. By this time the entire cloud-top region had begun to descend. The cloud top continued to descend was about 8.5 km (T ~ - 18 ºC) by 40 min. The ice concentration increased to 21.5 L^{-1} at cloud top.

The maximum values at each level in the control run of the vertical velocity, and the number concentrations of raindrops, graupel particles and ice crystals are shown in Figure 5. As the cloud developed, latent heat release and reduced water loading drove the increase in the vertical velocity (), the maximum reached 18.8 ms^{-1} at z = 5.55 km at 19 min. Raindrops developed after 7 min, and the maximum concentration was 330.4 L^{-1} at z = 3.45 km at 13 min. The major region of graupel particles appeared at an altitude of approximately 8 km at about 30 min, with the maximum being 1.7 L^{-1} at 8.7 km at 41 min. Additionally, a local maximum was at about 6 km and its value was 0.26 L^{-1} at 31 min. The major region of ice crystals occurred above an altitude of 8 km with a maximum 21.5 L^{-1} at z = 9.15 km at 61 min. In the HM zone, the maximum concentration was 4.1 L^{-1} at z = 6.6 km at 30 min, closely related to the local maximum in graupel concentration.

4.2 Maximum concentration in the HM zone

Figure 6 shows the temporal variation of the maximum concentration of ice in the HM zone for the control and sensitivity runs. Overall, the concentrations start to increase at about 20 min and reach the maximum values at about 30 min except in

the THERMALS run. The curve of concentrations for the THERMALS run is identical to that of CTL run before 45 min but greatly increases afterward.

The control run produced a maximum ice concentration of 4.1 L^{-1} which is significantly smaller than the observed value (> 40 L^{-1}). The Morrison microphysics scheme uses the Cooper parameterization for the primary ice production, which is based on a best fit curve of measurements from Wyoming wintertime cap clouds, wintertime orographic clouds of southwestern Colorado, Israel winter cumulus clouds, summertime cumulus clouds of Montana, cumulus clouds of South Africa; and Australian cumulus clouds. As discussed by Cooper (1986), the variance in the ice concentrations at any given temperature is large, probably due to the high variability in INP population itself or the wide variability in the activated fraction of INPs. Since the chemical and physical properties of INPs vary with time and space, the Cooper parameterization does not necessarily represent the INP conditions of the observed cloud. To investigate the impact of possible INP properties, such as the onset freezing temperature, the abundance of active INPs, and the freezing efficiency, on the ice concentration in the HM zone, as plotted in Figure 6, a series of sensitivity simulations were conducted. The maximum ice concentration is twice higher when the rate of ice production in the HM scheme is doubled. When the onset freezing temperature of the Cooper parameterization in the Morrison scheme is relaxed from the default value of -8 ℃ to -3 ℃ (RLX), the maximum concentration increased to 8.8 L^{-1}. If the ice number concentration produced with the Cooper parameterization is multiplied by 10 (TEN), the maximum concentration increased to 13.4L^{-1}. A combination of the relaxation and enhancement (RLXTEN) further increased the concentration in the HM zone to 30.6 L^{-1}. The maximum concentrations increase to 45.3 L^{-1} in RLX3x100 and 48.6 L^{-1} in RLX2x100. The DeMott scheme (DMTA) produced the maximum concentration of 11.7 L^{-1}. It increases to 32.2L^{-1} with relaxation (DMTRLX) and 40.4 L^{-1} with both relaxation and enhancement (DMTRLX2).

The maximum concentration in the HM zone decreases to 1.8 L^{-1} using the Paukert scheme (PAUKERT) without the dust layer being considered. Accounting for the dust layer (PAUKERTD) leads to only a slight increase to 1.9 L^{-1}.

Overall, the greater the staring freezing temperature, the higher the maximum ice concentration appears in the HM zone. Simulations with both relaxation and enhancement can produce similar concentrations of the secondary ice production to the observations made in some passes (e.g., ~ 50 L^{-1} in pass at approximately 5830 m in Figure 3), but much lower than the maximum value ~ 270 L^{-1} observed in the cloud.

The temporal variations of the ice production in the HM zone are broadly similar except for the two-thermal run (THERMALS) which produced a maximum concentration of 121 L^{-1} at 69 mins. We will discuss the causes of enhanced secondary ice production in the microphysical sensitivity runs next and in the dynamical sensitivity run later.

4.3 Onset freezing temperature and freezing efficiency

To investigate the causes of the change in secondary ice production due to different microphysical schemes, the differences of several microphysical properties between a sensitivity and the control simulations are shown in Figure 7. The reasons for the different concentrations of secondary ice between the RLXTEN and CTL runs are examined in the following analysis. There was a significantly higher concentration of secondary ice particles produced in TLXTEN compared to the CTL run. Figure 7 shows the detailed differences between the two runs. A banana-shaped area of positive difference in vertical velocity appears in Fig. 7a. The positive region increases with time and height from 23 min and z ~ 6.6 km, and the maximum is 2.7 m s^{-1} at 35 min at 9.15 km. The increases in the vertical velocity were most likely caused by the extra latent heat release due to the enhancement of freezing (e.g., McGee and van den Heever, 2014).

The region of the positive difference in the cloud mixing ratio is well correlated with the enhanced vertical motion before 35 min, indicating that the enhanced vertical velocity pushed the cloud top higher, which was confirmed with an inspection of the fields of the two simulations and their difference (figures now shown).

Although there is a small area of increase in the rain mixing ratio, the ratio generally tends to decrease mainly below 7 km and with the minimum at 24 min and z = 6.6 km. The decrease was a result of more raindrops being converted to graupel particles.

The maximum increase in the raindrop number concentration in RLXTEN is at 30 min and z = 8.55 km (Figure 7e). However, a decrease occurred after about 37 min and the minimum is above 8 km. This is because in the RLXTEN run, the axis of the contours is angled upwards, while it is downwards in the CTL run the axis in the CTL run goes down after 38 min. The enhanced vertical velocity in the RLXTEN run transported more cloud water and more raindrops above 7 km.

The mixing ratios of graupel and the ice crystals tend to increase (Figure 7c and d, respectively). The maximum increases appears at 24 min and z = 6.75 km and at 47 min and z = 9.45 km, respectively. The increase in the mixing ration of graupel seems to be related to the raindrops being converted to graupel by direct freezing since there is no increasei7 in ice particles at that time and altitude. The graupel number concentration increases (Figure 7f), with the maximum difference being at 39 min and z = 9.15 km.

Differences in the maximum ice crystal concentration at each model level as a function of time between all the sensitivity runs and the CTL are shown in Figure 8.

For the RLX run, the differences at the upper levels are small since the onset freezing temperature was only relaxed from -8 to -3 °C. However, the increase in the ice concentration in the HM zone is 5.9 L^{-1}. For the enhancement run TEN, the

concentration increases both in the upper levels and in the HM zone due to more primary ice production, and the latter is 13.4 L⁻¹. With both relaxation and enhancement, the increase in the HM zone is 30.6 L⁻¹. The relaxation leads to earlier secondary ice production and the enhancement increases ice production not only in the HM zone but also in the higher levels. The differences in concentrations further increase to 45.2 L⁻¹ in RLX3X100 and 48.5 L⁻¹ in RLX2X100, as expected.

300 There are more/less increases in the lower/upper levels when using the DeMott scheme (DMTA) because of the slope of DeMott curve, i.e., more IN at higher temperature. The ice concentration in the HM zone in DMTA is 11.6 L⁻¹. When the onset freezing temperature is relaxed from -8 to -3 ºC (DMTRLX), there are slight increase at the upper levels, but a larger increase in the HM zone (32.1 L⁻¹). With both relaxation and enhancement (DMTRLX2), the increase in the HM zone is even larger (40.3 L⁻¹), although not as large as in the RLX3X100 or RLX2X100.

305

The results indicate that combinations of relaxing the onset freezing temperature and enhancing the efficiency can produce secondary ice in concentration of several tens per litre. However, these concentrations are significantly less than the maximum concentration observed by the aircraft.

4.4 Dust particles as INP

310 It is interesting to consider if is it possible to reproduce the observed concentrations of ice particles via primary and secondary ice production processes if the INP are only dust particles? We used the Paukert scheme to address this question with two simulations (see Table 1). The differences in the vertical velocity between the PAUKERT CTL runs are less than 0.7 ms⁻¹ (Figure 9a). The number concentrations of raindrops, graupel particles, and ice crystals generally increased approximately above 8 km and decrease slightly below (Figures 9b-9d). There was less riming, therefore, less secondary ice

315 production in the HM zone. The decrease in the ice concentration in the HM zone was about 3 L⁻¹. This is because that the onset freezing temperature in the Paukert scheme was -12 ºC, less than the default value, -8 ºC, in the Morrison scheme. Freezing took place later in time and hence higher in altitude.

To account for the dust layer between 2 and 3 km (Figure 1), we modified the INP number to drop number ratio in the

320 Paukert scheme. However, the results indicate that there was an insignificant increase in the concentration of ice particles (figures not shown). The results of these two simulations suggest that dust alone is not enough to produce the secondary ice similar to the observations in this case.

4.5 Multiple thermals

The above results indicate that the different microphysical schemes affect the secondary ice production. None of them

325 produce a sufficient number of ice particles to explain the observation. Next, we will discuss the impact of the cloud dynamics on the secondary ice production in a cloud with multi-thermals. It would be incorrect not to consider both the

dynamics and microphysics and their interactions. Figure 10 shows the time-height variations of maximum values in the THERMALS run.

330   The defining feature of this run is the two updraughts (Fig. 10a). The isoline of 2 ms^{-1} of the first updraught started from the beginning at about 1 km and ended at about 35 min and reached an altitude of approximately 9 km, whilst the second started at about 20 min and also reached also approximately 9 km. There are no differences in the maximum vertical velocity in the first updraught before 20 min between the THERMALS and CTL runs. The difference in the first updraught is minimal (< 0.5 m s^{-1}) and appears beyond 20 min. Although the maximum vertical velocity in the second updraught was smaller, the

335   updraught lasted for the longer time of approximately 30 min.

There is virtually no difference in the raindrop concentration associated with the first updraught. However, there are two local maxima associated with the second updraught: one between 30 – 40 min at z = 2 – 4 km, and the other between 50 – 60 min at z = 7 – 9 km. In the control run, many raindrops precipitated before 20 min (Figure 5b). Some raindrops were

340   transferred to graupel particles via direct freezing, but there left some near the cloud top (e.g., Figure 4c). In the multiple thermal run, the second thermal started 20 min from the beginning. The lower-level maximum around 30 - 40 min was related to raindrops developed with the second thermal. There was a second maximum at z = 7 – 9 (e.g., Figure 11).

There are very little differences in the graupel concentration between the THERMALS run and the CTL run before 45 min

345   by comparing Figures 5a and 10a. However, two maxima appeared at 60 min and 75 min between 7 and 8 km with the multi-thermal run. The graupel concentrations are much higher, 12 and 17 L^{-1}, compared to less than 2 L^{-1} at about 40 min in the CTL run, which indicates more riming in the THERMALS run. Similarly, there are very little changes in the ice crystal concentration before 45 min. Associated with the two graupel maxima, there are two ice crystal maxima: one being 84.9 L^{-1} at 58 min and z = 6.9 km and the other 121 L^{-1} at 69 min and z = 6.75 km.

350

Figure 11 presents a time sequence of cloud properties for the THERMAL run between 54 – 69 min at intervals of 3 min spanning a period of a maximum of the secondary ice production in the HM zone.

A turret containing graupel reached just above 8 km at x ≈ 7 km with strong updraught up to 7.6 ms^{-1} and raindrops below

355   the turret at 54 min. The turret developed to a slightly higher level at 57 min and started to collapse, but strong updraughts of 7.8 ms^{-1} below the turret still supported the graupel particles from falling down into the HM zone. As the turret continued to collapse and the updraughts below the turret weakened, graupel particles fell down into the HM zone at 60 min. A local maximum of ice concentration appeared around 7 km in altitude and x ≈ 7.2 km, which was produced by the HM process. During the next 9 min, the coexistence of graupel particles, drops and raindrops produced secondary ice particles in the zone

360 to 121 L⁻¹. More riming and hence secondary ice particles were produced in the second thermal due to the increase in liquid

water content in the updraught.

5. Discussions

Firstly, we discuss if the conditions for the rime-splintering process were met in cloud penetrations. Figure 12 shows the

variations of the aircraft measured vertical velocity and the cloud drop concentration at 6180 m between 15:12:07 and

365 15:15:39 UTC. The vertical velocities indicate the weak updraught in the cloud was surrounded by downdraughts. The

vertical velocities were approximate 2 ms⁻¹ at the time when columns were measured (Figure 13). The concentrations of

drops in the cloud were a few tens per cubic centimetre (Fig. 12d). In Figure 13, graupel particles, small droplets and large

drops were observed during the same pass as in Figure 12. Fragments of frozen drops were found, but not in a great amount

(figures not shown). The high concentrations of ice particles were most likely produced by the rime-splintering process

370 because all the conditions for the process were met. However, there is no causal evidence and we cannot rule out other

mechanisms of secondary ice production.

Another question is that whether very active (e.g, biogenic) INPs existed in the environment of the observed clouds (Lloyd et

al., 2020). As described in Section 2, the aerosol particles in the lowest 1.5 km were mostly marine with some polluted dust,

375 and the upper layer at 2 – 3 km consisted mostly of dust. The laser ablation aerosol particle time-of-flight mass spectrometer

(LAAPTOF), was deployed to measure aerosol properties during the field campaign. The organic-biogenic fractions were

moderately high in the measured dust particles at the Praia airport on 21 August (Marsden et al., 2018), which could affect

the ice formation in the clouds. Although the ground measurement site was about 150 km away from the clouds, it is possible

that aerosol particles in the aircraft operation region had similar chemical composition to those in the ground site.

380

It is noted that other mechanisms of secondary ice production may have operated in these clouds, such as fragmentation

during evaporation (Bacon et al. 1998), crystal-crystal collision (Takahashi et al., 1995), fragile needles combined with ice–

ice collision fragmentation (Knight, 2012), shattering following the freezing of supercooled raindrops (Leisner et al., 2014,

Wildeman et al., 2017). The shattering mechanism may be most efficient between -10 ºC and -15 ºC. Although the Knight

385 mechanism operates at the similar temperature range, there is no parameterization of the process. Since the tops of the clouds

in this study were no higher than -10 ºC and the conditions in the clouds were conducive to the HM process as currently

understood, we have focussed on modelling the production of ice particles by that rime-splintering process.

5. Conclusions

390 Numerical simulations of the 21 August 2015 ICE-D deep convective clouds in the Cape Verde region examined the secondary ice production through the riming-splintering process and the sensitivity to the onset freezing temperature or/and freezing efficiency, as well as the impact of multiple thermals.

CM1 was run for the 21 August case. The Morrison microphysics scheme was applied for the control run. Additional
395 simulations were run with adjusted onset freezing temperature, freezing efficiency, and the Paukert scheme for dust alone INPs, and a two-thermal simulation. The control simulation produced a maximum concentration of secondary ice a few per litre in the HM temperature zone which is much lower than the observed value. One possible reason for the underestimation is that the default onset freezing temperature is -8 ℃, which means the first ice in the control run appeared too late at higher levels. Relaxing the onset temperature from -8 to -3 ℃ doubled the maximum concentration of the secondary ice, but is still
400 not as high as the observed. Enhancing the freezing efficiency made more primary ice particles and tripled the maximum concentration, which is still not enough. Some combinations of the relaxation and enhancement lead to higher concentrations of secondary ice close to the observations. The results suggest that more active INPs with higher onset freezing temperatures are needed to produce similar amounts of secondary ice. It is possible that INPs in this case might include k-rich feldspar aerosol particles or/and dust particles attached with biogenic INPs of high onset freezing temperatures, such as bacteria.

405

The simulations with the Paukert schemes to consider the cases with dust alone INPs had secondary ice production even lower than the control simulation. Because the onset freezing temperature in the Paukert scheme is lower than in the Morrison scheme, the primary ice appeared late at higher altitude, which resulted in reduced graupel in the HM zone, and hence, decreases in the secondary ice production. Dust INPs alone are not enough to produce similar amounts of secondary
410 ice.

In the multiple thermal run, the secondary ice production associated with the first thermal is identical to that in the control run. However, the secondary ice concentration associated with the second thermal is much higher. The reason for the much more secondary ice is because the second thermal produces freshly formed drops and raindrops in the HM zone for graupel particles to collect and promotes the riming-splintering process. The cloud dynamics is also important in secondary ice
415 production. The multiple thermal simulation still cannot produce the highest observed ice number concentration.

A thorough explanation of the secondary ice production faces several challenges. The first challenge is the measurement of secondary ice particles, particularly for newly formed very small ice particles which is hard to be discriminated although new probes, such as small ice detectors have been developed (Baumgardner et al., 2017). The second is the measurement of
420 the full spectra of all INPs and CCN (Kanji et al., 2017). The third is the identification of mechanisms of secondary ice

production (Field et al., 2017). The fourth challenge is the dynamics (Field et al., 2017). The development of new instruments and techniques will help improve our understanding of secondary ice production.

Code availability: The CM1 model is available at https://www2.mmm.ucar.edu/people/bryan/cm1.

425 **Author contribution:** ZC designed the experiments and performed the simulations. GL analysed the ice particle concentrations. ZC and AB prepared the manuscript with contributions from all co-authors.

Competing interests: The authors declare that they have no conflict of interest.

Acknowledgements: This project was funded by UK's Natural Environment Research Council (NE/M00340X/1). NCEP Reanalysis data were provided by the NOAA/OAR/ESRL PSD, Boulder, Colorado, USA, from their Web site at

430 https://www.esrl.noaa.gov/psd/. We are grateful to Dr. George Bryan for his development and maintenance of CM1. The BAe-146 aircrew and instrument operators are greatly appreciated. ZC is partly funded by The Centre for Environmental Modelling And Computation (CEMAC), University of Leeds.

References

435 Bacon, N. J., Swanson, B. D., Baker, M. B., and Davis, E. J.: Breakup of levitated frost particles, J. Geophys. Res., 103, 13763–13775, https://doi.org/10.1029/98JD01162, 1998.

Baumgardner, D., Abel, S. J., Axisa, D., Cotton, R., Crosier, J., Field, P., Gurganus, C., Heymsfield, A., Korolev, A., Krämer, M., Lawson, P., McFarquhar, G., Ulanowski, Z., and Um, J.: Cloud Ice Properties: In Situ Measurement Challenges, Meteor. Mon., 58, 9.1–9.23, https://doi.org/10.1175/AMSMONOGRAPHS-D-16-0011.1, 2017.

440 Blyth, A. M., Cooper, W. A., and Jensen, J. B.: A Study of the Source of Entrained Air in Montana Cumuli, J. Atmos. Sci., 45, 3944–3964, 1988.

Blyth, A. M. and Latham, J.: A multi-thermal model of cumulus glaciation via the Hallett-Mossop process, Q. J. Roy. Meteorol. Soc., 123, 1185–1198, 1997.

Bryan, G. H., Wyngaard, J. C., and Fritsch, J. M.: Resolution Requirements for the Simulation of Deep Moist Convection,

445 Mon. Weather Rev., 131, 2394–2416, 2003.

Bryan, G. H., and Morrison, H.: Sensitivity of a simulated squall line to horizontal resolution and parameterization of microphysics. Mon. Wea. Rev., **140**, 202–225, doi:https://doi.org/10.1175/MWR-D-11-00046.1, 2012.

Burrows, S. M., Hoose, C., Pöschl, U., and Lawrence, M. G.: Ice nuclei in marine air: biogenic particles or dust?, Atmos. Chem. Phys., 13, 245–267, https://doi.org/10.5194/acp-13-245-2013, 2013.

450 Cooper, W. A.: Ice initiation in natural clouds, in: Precipitation Enhancement—A Scientific Challenge, Springer, 29-32, 1986.

Crawford, I., Bower, K. N., Choularton, T. W., Dearden, C., Crosier, J., Westbrook, C., Capes, G., Coe, H., Connolly, P. J., Dorsey, J. R., Gallagher, M. W., Williams, P., Trembath, J., Cui, Z., and Blyth, A.: Ice formation and development in aged, wintertime cumulus over the UK: observations and modelling, Atmos. Chem. Phys., 12, 4963-4985, https://doi.org/10.5194/acp-12-4963-2012, 2012.

Crosier, J., Bower, K. N., Choularton, T. W., Westbrook, C. D., Connolly, P. J., Cui, Z. Q., Crawford, I. P., Capes, G. L., Coe, H., Dorsey, J. R., Williams, P. I., Illingworth, A. J., Gallagher, M. W., and Blyth, A. M.: Observations of ice multiplication in a weakly convective cell embedded in supercooled mid-level stratus, Atmos. Chem. Phys., 11, 257-273, https://doi.org/10.5194/acp-11-257-2011, 2011.

Cui, Z., Davies, S., Carslaw, K. S., and Blyth, A. M.: The response of precipitation to aerosol through riming and melting in deep convective clouds, Atmos. Chem. Phys., 11, 3495-3510, https://doi.org/10.5194/acp-11-3495-2011, 2011.

Cui, Z., Blyth, A. M., Bower, K. N., Crosier, J., and Choularton, T.: Aircraft measurements of wave clouds, Atmos. Chem. Phys., 12, 9881–9892, https://doi.org/10.5194/acp-12-9881-2012, 2012.

Cui, Z., Gadian, A., Blyth, A., Crosier, J., and Crawford, I.: Observations of the variation in aerosol and cloud microphysics along the 20_ S transect on 13 November 2008 during VOCALS-REx, J. Atmos. Sci., 2927–2943, doi:10.1175/JAS-D-13-0245.1, 71, 2014.

Damiani, R., Vali, G., and Haimov, S.: The Structure of Thermals in Cumulus from Airborne Dual-Doppler Radar Observations. *J. Atmos. Sci.,* **63**, 1432–1450, https://doi.org/10.1175/JAS3701.1, 2006

DeMott, P. J., Hill, T. C. J., McCluskey, C. S., Prather, K. A., Collins, D. B., Sullivan, R. C., Ruppel, M. J., Mason, R. H., Irish, V. E., Lee, T., Hwang, C. Y., Rhee, T. S., Snider, J. R., McMeeking, G. R., Dhaniyala, S., Lewis, E. R., Wentzell, J. J. B., Abbatt, J., Lee, C., Sultana, C. M., Ault, A. P., Axson, J. L., Diaz Martinez, M., Venero, I., Santos-Figueroa, G., Stokes, M. D., Deane, G. B., Mayol-Bracero, O. L., Grassian, V. H., Bertram, T. H., Bertram, A. K., Moffett, B. F., and Franc, G. D.: Sea spray aerosol as a unique source of ice nucleating particles, P. Natl. Acad. Sci. USA, 113, 5797–5803, https://doi.org/10.1073/pnas.1514034112, 2016.

Field, P. R., Lawson, R. P., Brown, P. R. A., Lloyd, G., Westbrook, C., Moisseev, D., Miltenberger, A., Nenes, A., Blyth, A., Choularton, T., Connolly, P., Buehl, J., Crosier, J., Cui, Z., Dearden, C., DeMott, P., Flossmann, A., Heymsfield, A., Huang, Y., Kalesse, H., Kanji, Z. A., Korolev, A., Kirchgaessner, A., LasherTrapp, S., Leisner, T., McFarquhar, G., Phillips, V., Stith, J., and Sullivan, S.: Secondary Ice Production: Current State of the Science and Recommendations for the Future, Meteor. Monogr., 58, 7.1–7.20, https://doi.org/10.1175/AMSMONOGRAPHS-D16-0014.1, 2017.

Garimella, S., Rothenberg, D. A., Wolf, M. J., David, R. O., Kanji, Z. A., Wang, C., Rösch, M., and Cziczo, D. J.: Uncertainty in counting ice nucleating particles with continuous flow diffusion chambers, Atmos. Chem. Phys., 17, 10855–10864, https://doi.org/10.5194/acp-17-10855-2017, 2017.

Hallett, J. and Mossop, S. C.: Production of secondary ice particles during the riming process, Nature, 249, 26–28, https://doi.org/10.1038/249026a0, 1974.

485 Hawker, R. E., Miltenberger, A. K., Wilkinson, J. M., Hill, A. A., Shipway, B. J., Cui, Z., Cotton, R. J., Carslaw, K. S., Field, P. R., and Murray, B. J.: The temperature dependence of ice-nucleating particle concentrations affects the radiative properties of tropical convective cloud systems, Atmos. Chem. Phys., 21, 5439–5461, https://doi.org/10.5194/acp-21-5439-2021, 2021.

Heiblum, R. H., Altaratz, O., Koren, I., Feingold, G., Kostinski, A. B., Khain, A. P., Ovchinnikov, M., Fredj, E., Dagan, G., and Pinto, L.: Characterization of cumulus cloud fields using trajectories in the center of gravity versus water mass phase

490 space: 1. Cloud tracking and phase space description, J. Geophys. Res., 121, 6336–6355, 2016.

Heus, T., Jonker, H., Van den Akker, H., Griffith, E., Koutek, M., and Post, F.: A statistical approach to the life cycle analysis of cumulus clouds selected in a virtual reality environment, J. Geophys. Res., 114, D06208, doi:10.1029/2008JD010917, 2009.

Heymsfield, A. J., Field, P. R., Bailey, M., Rogers, D. C., Stith, J., Twohy, C.,Wang, Z., and Haimov, S.: Ice in Clouds

495 Experiment-Layer Clouds. Part I: Ice growth rates derived from lenticular wave cloud penetrations, J. Atmos. Sci., 68, 2628–2654, 2011.

Heymsfield, A. and Willis, P.: Cloud conditions favoring secondary ice particle production in tropical maritime convection, J. Atmos. Sci., 71, 4500–4526, https://doi.org/10.1175/JAS-D-14-0093.1, 2014.

Hobbs, P. V. and Rangno, A. L.: Rapid development of high ice particle concentrations in small polar maritime cumuliform

500 cloud, J. Atmos. Sci., 47, 2710–2722, 1990.

Kanji, Z. A., Ladino, L. A., Wex, H., Boose, Y., Burkert-Kohn, M., Cziczo, D. J., and Krämer, M.: Overview of ice nucleating particles, Meteor. Mon., 58, 1.1–1.33, https://doi.org/10.1175/amsmonographs-d-16-0006.1, 2017.

Kaufmann, L., Marcolli, C., Hofer, J., Pinti, V., Hoyle, C. R., and Peter, T.: Ice nucleation efficiency of natural dust samples in the immersion mode, Atmos. Chem. Phys., 16, 11177-11206,

505 https://doi.org/10.5194/acp-16-11177-2016, 2016.

Keller, V. W., and Sax, R. I.: Microphysical development of a pulsating cumulus tower. *Quart. J. Roy. Meteor. Soc.*, 107, 679–697, 1981.

Kiselev, A., Bachmann, F., Pedevilla, P., Cox, S. J., Michaelides, A., Gerthsen, D., and Leisner, T.: Active sites in heterogeneous ice nucleation – the example of K-rich feldspars, Science, 355, 367–371,

510 https://doi.org/10.1126/science.aai8034, 2017.

Knight, C. A.: Ice Growth from the Vapor at −5°C, J. Atmos. Sci., 69, 2031–2040, 2012.

Knippertz, P., Tesche, M., Heinold, B., Kandler, K., Toledano, C., and Esselborn, M.: Dust mobilization and aerosol transport from West Africa to Cape Verde–A meteorological overview of SAMUM-2, Tellus B, 63, 430–447, doi:10.1111/j.1600-0889.2011.00544.x., 2011.

515 Koenig, L. R.: The glaciating behavior of small cumulonimbus clouds, J. Atmos. Sci., 20, 29–47, https://doi.org/10.1175/1520-0469(1963)020<0029:tgbosc>2.0.co;2, 1963.

Lawson, P. R., O'Connor, D., Zmarzly, P., Weaver, K., Baker, B.,and Mo, Q.: The 2D-S (stereo) probe: design and preliminarytests of a new airborne high-speed, high resolution particle imagineprobe, J. Atmos. Ocean. Tech., 23, 1462–1477, 2006.

520 Leisner, T., Pander, T., Handmann, P., and Kiselev, A.: Secondary ice processes upon heterogeneous freezing of cloud droplets, 14th Conf. on Cloud Physics and Atmospheric Radiation, June 2014, Boston, MA, USA, Amer. Meteor. Soc., 2.3, 2014.

Liu, D., Taylor, J. W., Crosier, J., Marsden, N., Bower, K. N., Lloyd, G., Ryder, C. L., Brooke, J. K., Cotton, R., Marenco, F., Blyth, A., Cui, Z., Estelles, V., Gallagher, M., Coe, H., and Choularton, T. W.: Aircraft and ground measurements of dust
525 aerosols over the west African coast in summer 2015 during ICE-D and AER-D, Atmos. Chem. Phys., 18, 3817–3838, https://doi.org/10.5194/acp-18-3817-2018, 2018.

Marenco, F.: Nadir airborne lidar observations of deep aerosol layers, Atmos. Meas. Tech., 6, 2055–2064, https://doi.org/10.5194/amt-6-2055-2013, 2013.

Lloyd, G., Choularton, T., Bower, K., Crosier, J., Gallagher, M., Flynn, M., Dorsey, J., Liu, D., Taylor, J. W., Schlenczek, O.,
530 Fugal, J., Borrmann, S., Cotton, R., Field, P., and Blyth, A.: Small ice particles at slightly supercooled temperatures in tropical maritime convection, Atmos. Chem. Phys., 20, 3895–3904, https://doi.org/10.5194/acp-20-3895-2020, 2020.

Marsden, N. A., Ullrich, R., Möhler, O., Eriksen Hammer, S., Kandler, K., Cui, Z., Williams, P. I., Flynn, M. J., Liu, D., Allan, J. D., and Coe, H.: Mineralogy and mixing state of north African mineral dust by online single-particle mass spectrometry, Atmos. Chem. Phys., 19, 2259–2281, https://doi.org/10.5194/acp-19-2259-2019, 2019.

535 McFarquhar, G. M., Baumgardner, D., and Heymsfield, A. J.: 0 - Background and Overview, Meteor. Mon., 58, v–ix, https://doi.org/10.1175/AMSMONOGRAPHS-D-16-0018.1, 2017.

McGee, C. J. and van den Heever, S. C.: Latent Heating and Mixing Due to Entrainment in Tropical Deep Convection, J. Atmos. Sci., 71, 816–832, doi:10.1175/JAS-D-13-0140.1, 2014.

Nickovic, S., Vukovic, A., Vujadinovic, M., Djurdjevic, V., and Pejanovic, G.: Technical Note: High-resolution mineralogical
540 database of dust-productive soils for atmospheric dust modeling, Atmos. Chem. Phys., 12, 845-855, https://doi.org/10.5194/acp-12-845-2012, 2012.

Oraltay, R. G. and Hallett, J.: Evaporation and melting of ice crystals: A laboratory study, Atmos. Res., 24(1–4), 169–189, doi:10.1016/0169-8095(89)90044-6, 1989.

Paukert, M. and Hoose, C.: Modeling immersion freezing with aerosol-dependent prognostic ice nuclei in Arctic mixedphase
545 clouds, J. Geophys. Res.-Atmos., 119, 9073–9092, https://doi.org/10.1002/2014JD021917, 2014.

Phillips, V. T., Yano, J.-I., and Khain, A.: Ice multiplication by break-up in ice-ice collisions. Part I: Theoretical formulation, J. Atmos. Sci., 74, 1705–1719, doi:10.1175/JAS-D-16-0224.1, 2017.

Price, H. C., Baustian, K. J., McQuaid, J. B., Blyth, A., Bower, K. N., Choularton, T., Cotton, R. J., Cui, Z., Field, P. R., Gallagher, M., Hawker, R., Merrington, A., Miltenberger, A., Neely III, R. R., Parker, S. T., Rosenberg, P. D., Taylor, J. W.,
550 Trembath, J., Vergara-Temprado, J., Whale, T. F., Wilson, T. W., Young, G., and Murray, B. J.: Atmospheric Ice-Nucleating Particles in the Dusty Tropical Atlantic, J. Geophys. Res.-Atmos., 123, 2175– 2193, https://doi.org/10.1002/2017JD027560, 2018.

Seinfeld, J. H., Bretherton, C., Carslaw, K. S., Coe, H., DeMott, P. J., Dunlea, E. J., Feingold, G., Ghan, S., Guenther, A. B., Kahn, R., Kraucunas, I., Kreidenweis, S. M., Molina, M. J., Nenes, A., Penner, J. E., Prather, K. A., Ramanathan, V.,

555 Ramaswamy, V., Rasch, P. J., Ravishankara, A. R., Rosenfeld, D., Stephens, G., and Wood, R.: Improving our fundamental understanding of the role of aerosol–cloud interactions in the climate system, P. Natl. Acad. Sci. USA, 113, 5781–5790, doi:10.1073/pnas.1514043113, 2016.

Storelvmo, T.: Aerosol Effects on Climate via Mixed-Phase and Ice Clouds, Annu. Rev. Earth Planet. Sci., 45, 199–222, https://doi.org/10.1146/annurev-earth-060115-012240, 2017.

560 Takahashi, T., Nagao, Y., and Kushiyama, Y.: Possible high ice particle production during graupel-graupel collisions, J. Atmos. Sci., 52, 4523–4527, https://doi.org/10.1175/1520-0469, 1995.

Wildeman, S., Sterl, S., Sun, C. and Lohse, D.: Fast Dynamics of Water Droplets Freezing from the Outside In, Phys. Rev. Lett., 118(8), 84101, doi:10.1103/PhysRevLett.118.084101, 2017.

565 Wilson, T. W., Ladino, L. A., Alpert, P. A., Breckels, M. N., Brooks, I. M., Burrows, S. M., Carslaw, K. S., Huffman, J. A., Judd, C., Kilthau, W. P., Mason, R. H., McFiggans, G., Miller, L. A., Najera, J. J., Polishchuk, E., Rae, S., Schiller, C. L., Si, M., Vergara Temprado, J., Whale, T. H., Wong, J. P. S., Wurl, O., Yakobi-Hancock, J. D., Abbatt, J. P. D., Aller, J. Y., Bertram, A. K., Knopf, D. A., and Murray, B. J..: A marine biogenic source of atmospheric ice-nucleating particles, Nature, 525, 234–238, https://doi.org/10.1038/nature14986, 2015.

570   **Table 1. Experimental design**

Experiment	Description
CTL	The control run using the Morrison scheme
HM2	Same as CTL, except the rate of the HM process is doubled
RLX	Same as CTL, except the onset freezing temperature being -3 ºC, rather than -8 ºC
TEN	The ice concentration from the Cooper scheme is multiplied by 10
RLXTEN	Combination of RLX and TEN
RLX3X100	The onset freezing temperature being -3 ºC and the ice concentration is multiplied by 100
RLX2X100	The onset freezing temperature being -2 ºC and the ice concentration is multiplied by 100
DMTA	Use DeMott et al. (2010) best fit for all data, $0.117 \exp(-0.125*(TK - 273.2))$, with the onset freezing tempearture being -8 ºC
DMTRLX	Same as DMTA, but the staring freezing Temperature is -3 ºC
DMTRLX2	Same as DMLRLX, but the ice concentration is multiplied by 2
PAUKERT	Paukert scheme
PAUKERTD	Same as PAUKERT, but the ice concentration is enhanced in the dust layer
THERMALS	A second bubble of 2 ºC is imposed at 20 min from simulation
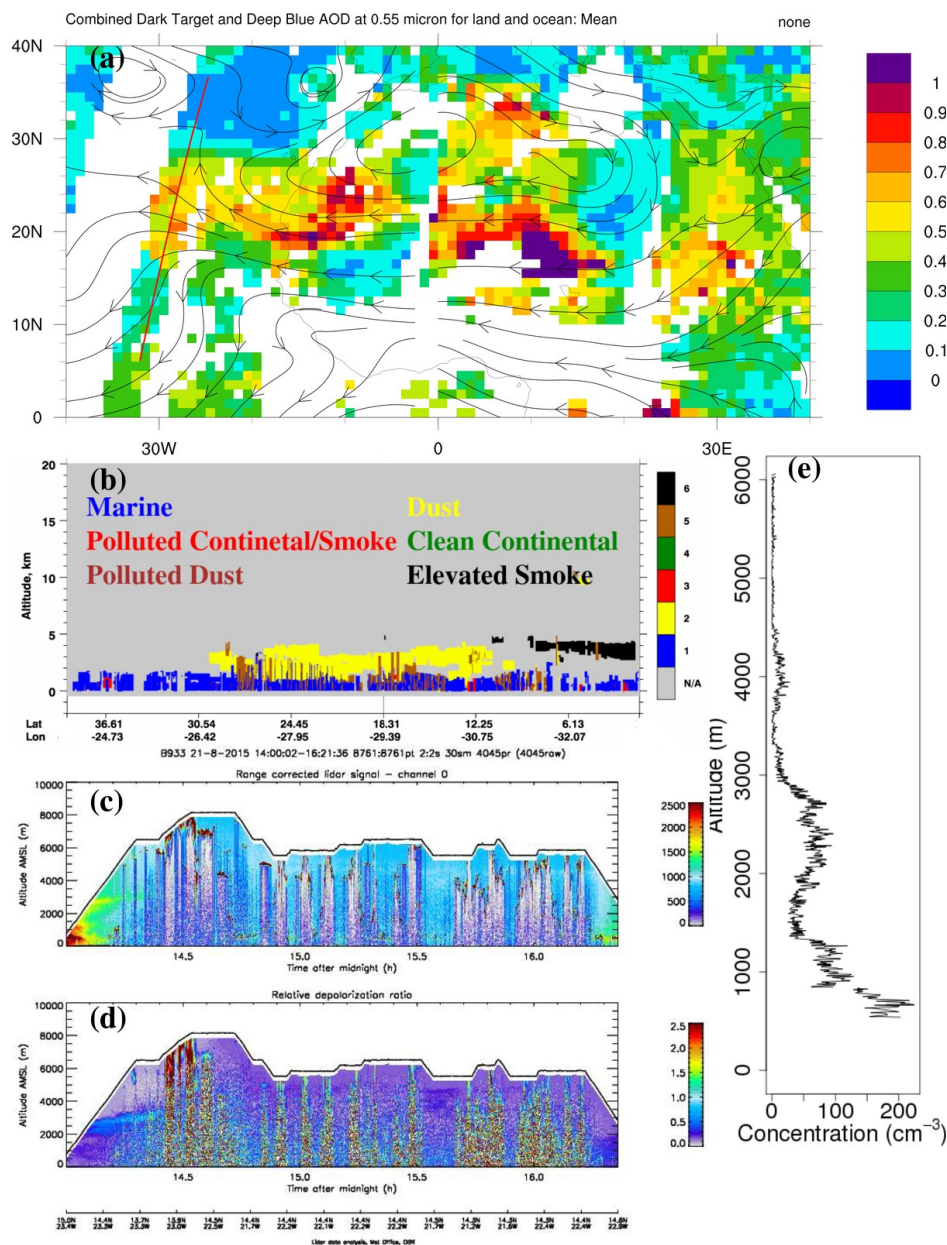
575

Figure 1. (a) MODIS combined Dark Target and Deep Blue mean AOD at 0.55 µm for land and ocean on 21 August 2015, with the red line representing the path of the CALIPSO, (b) CALIPSO aerosol subtypes on 21 August 2015, (c) range correlated lidar signal and (d) relative depolarization ratio measured with the UK Met Office's Lidar on board the BAe 146 aircraft, (e) vertical variation of aerosol concentration measured with the PCASP on board the BAe 146 aircraft.

580

585

590
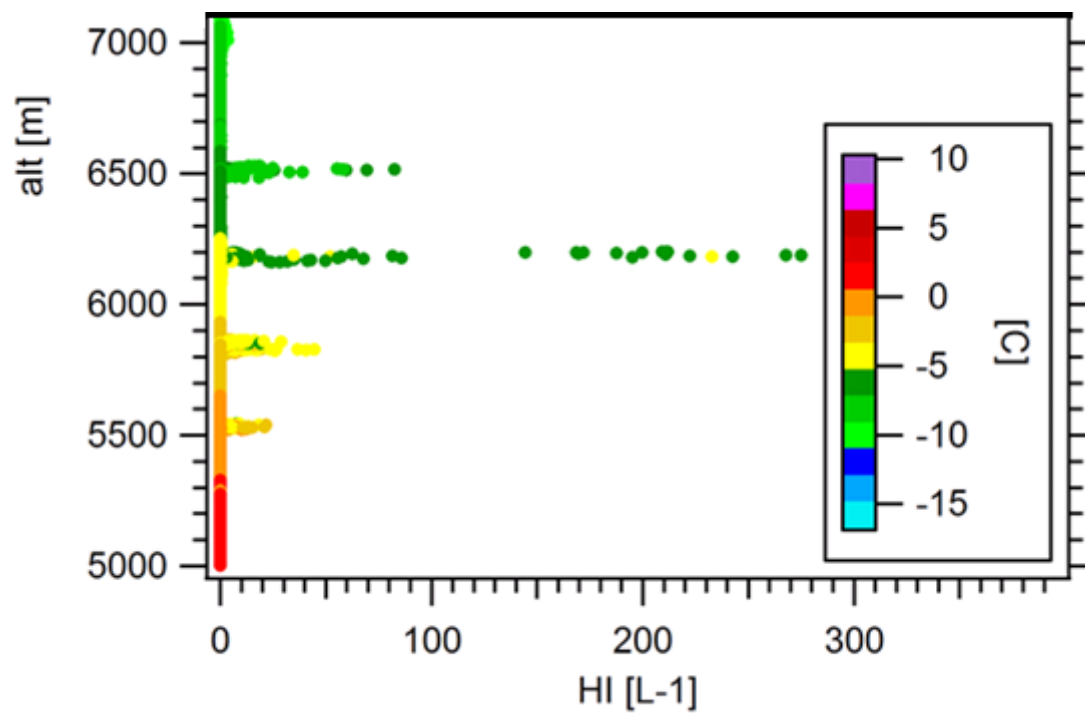
Figure 2. Ice concentration as a function of altitude as measured with the 2DS probe on board the Bae 146 aircraft.

595
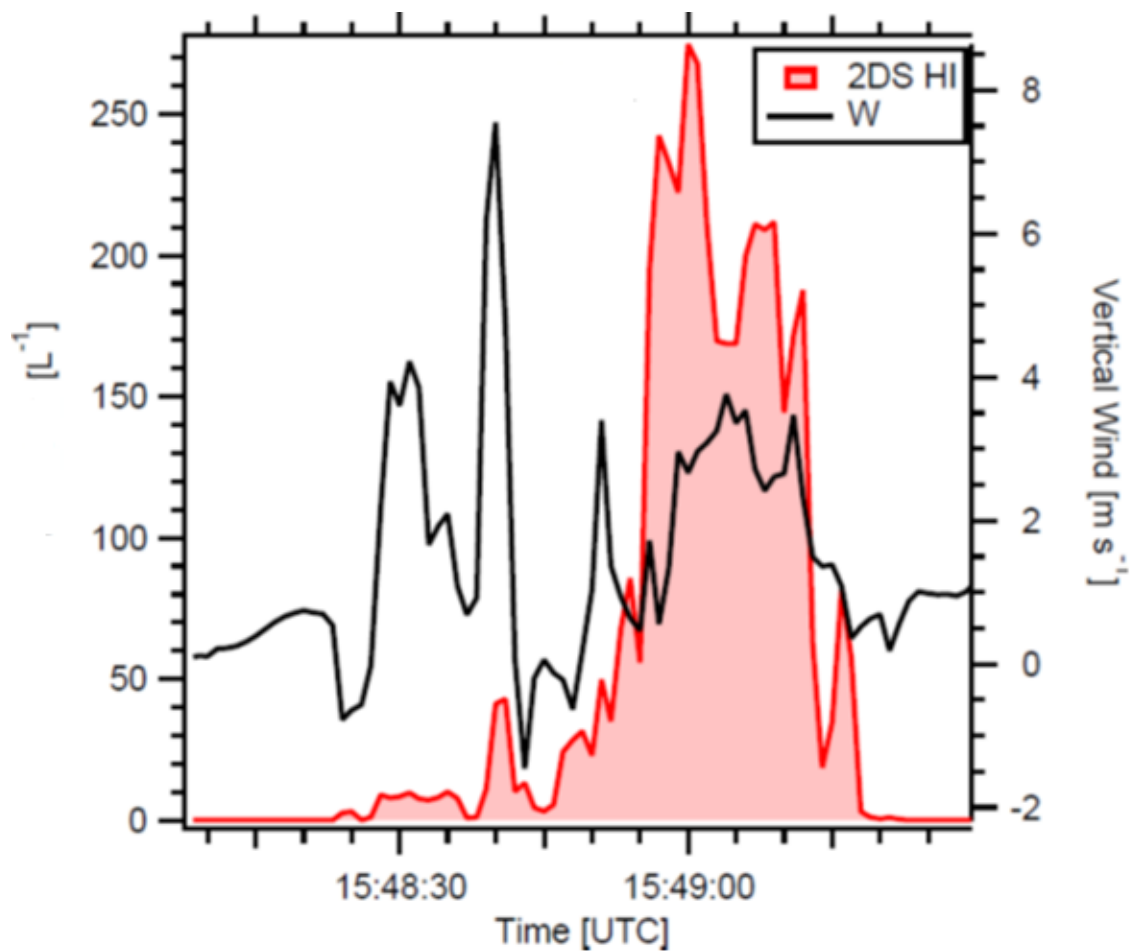
Figure 3, Time series of the concentration of ice particles (L^{-1}) and vertical velocity (ms^{-1}) between 15:48:05 UTC and 15:49:30 UTC on 21 August 2015.

600
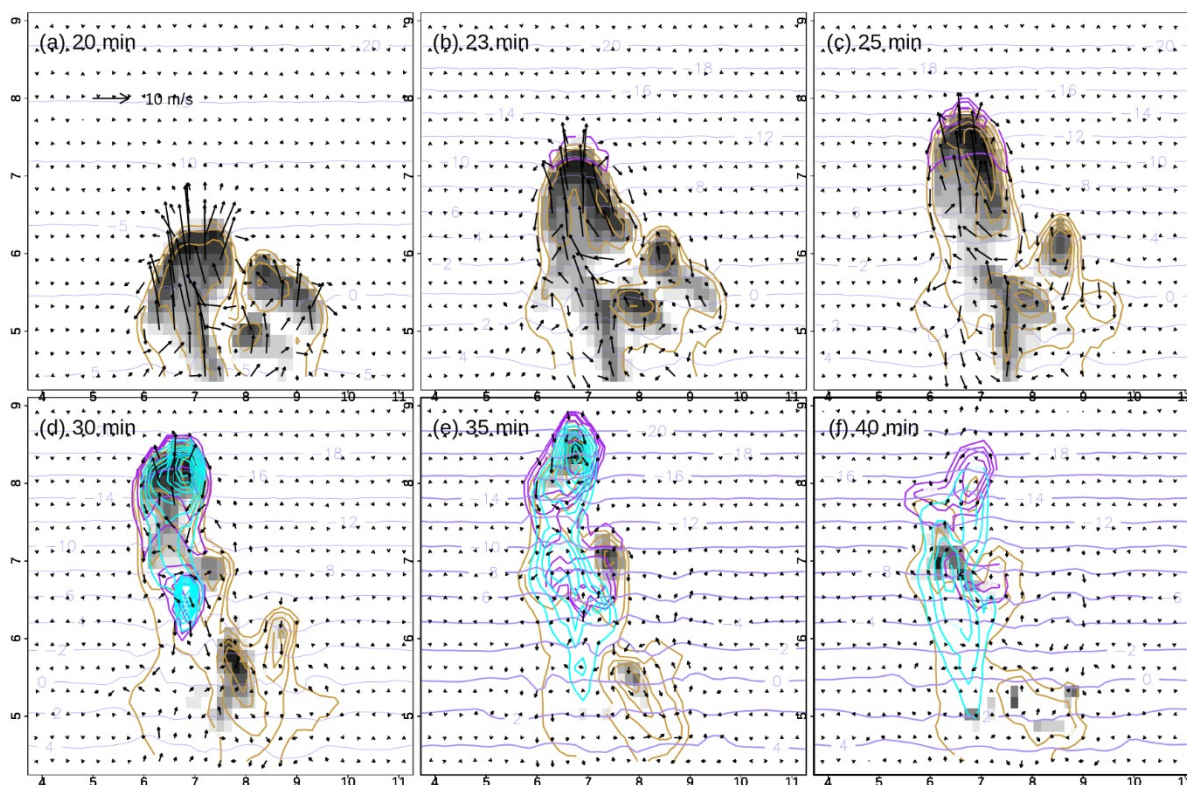
Figure 4. Time sequence for the control run CTL of spatial distribution of wind vectors, concentration of raindrops, ice crystals, and graupel particles at (a) 20 min, (b) 23 min, (c) 25 min, (d) 30min, (e) 35min and (f) 40 min. The orange, pupple and cyan lines are the concentration of raindrops (contours at 1, then 2.5 to 10 in intervals of 2.5, then in intervals of 5 to 70 L^{-1}), ice crystals (contours at 0.25, 0.5, 1, 2.5, 5, 7.5, 10, 12.5, 15, 17.5, 20, 22.5L^{-1}), and graupel particles (contour at 0.02L^{-1}), respectively. The shade represents cloud drop mixing ratio in each panel. The x-axis and y-axis are distance (km) and altitude (km), respectively. Also shown in each panel are the maximum concentrations and scale of the wind vectors. Isotherms are in ºC.
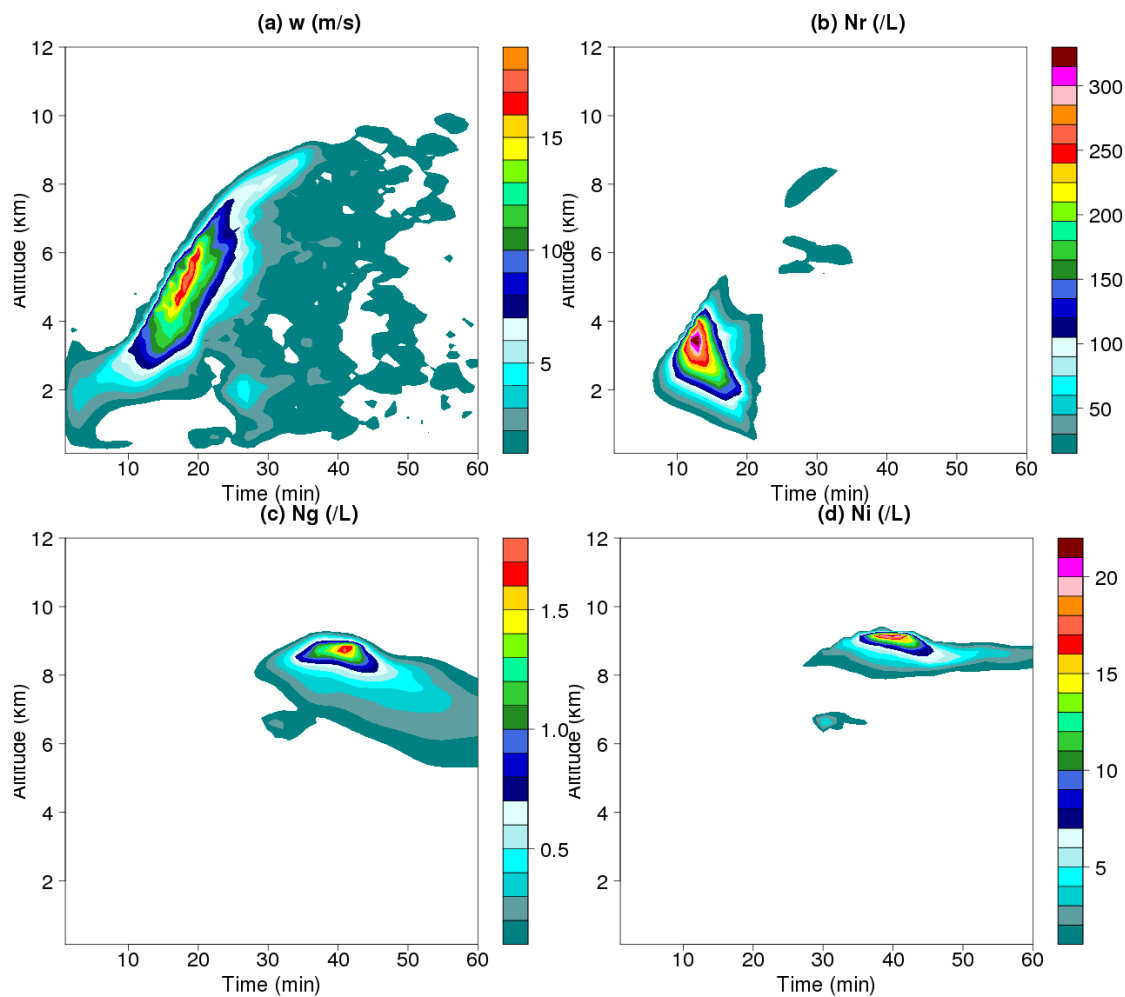
Figure 5. Time-height variations of maximum values in vertical velocity (a), raindrop concentration (b), graupel particle concentration (c), and ice crystal concentration (d) in the control run (CTL).

615
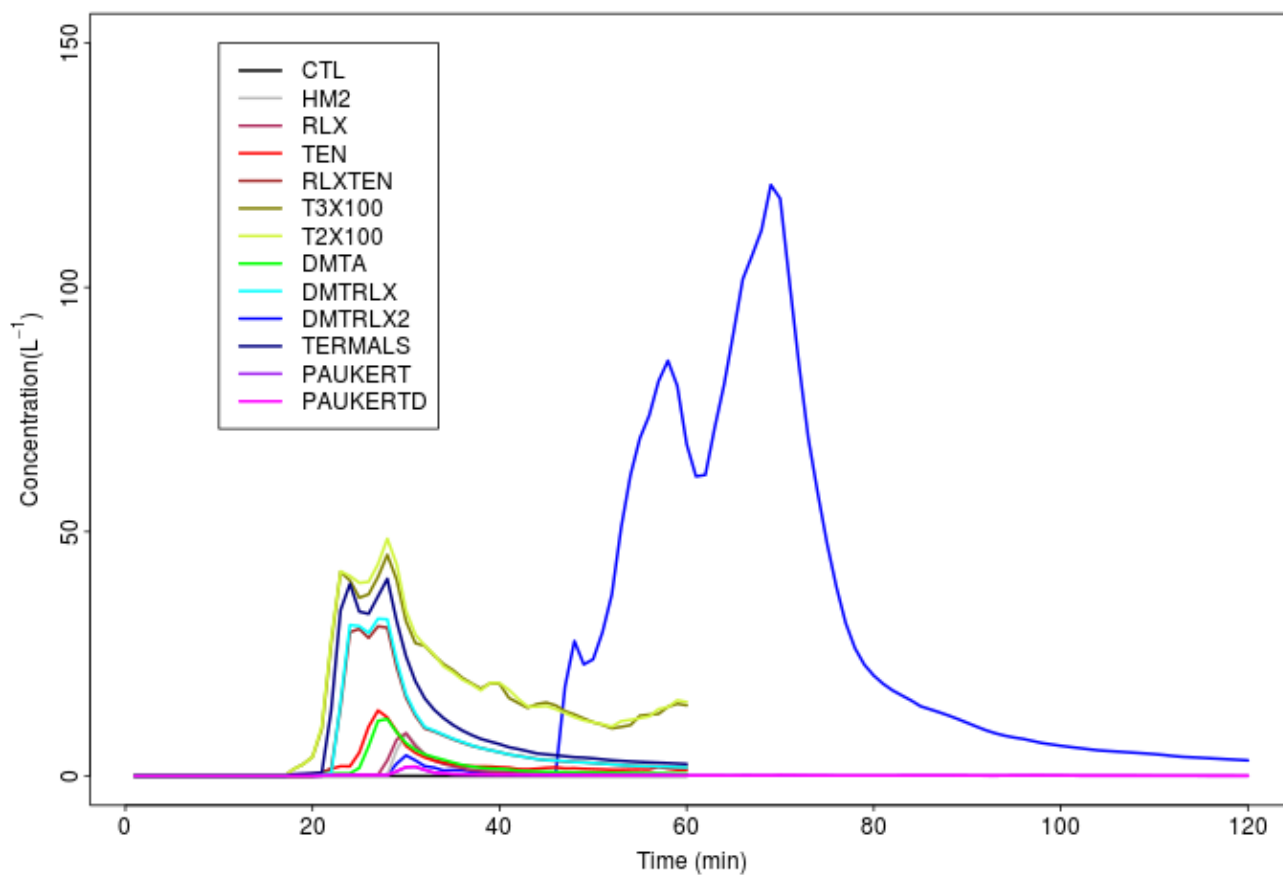
Figure 6. Temporal variation of maximum concentrations of ice crystals in the Hallett-Mossop temperature zone.

ction started: 27 May 2021

620
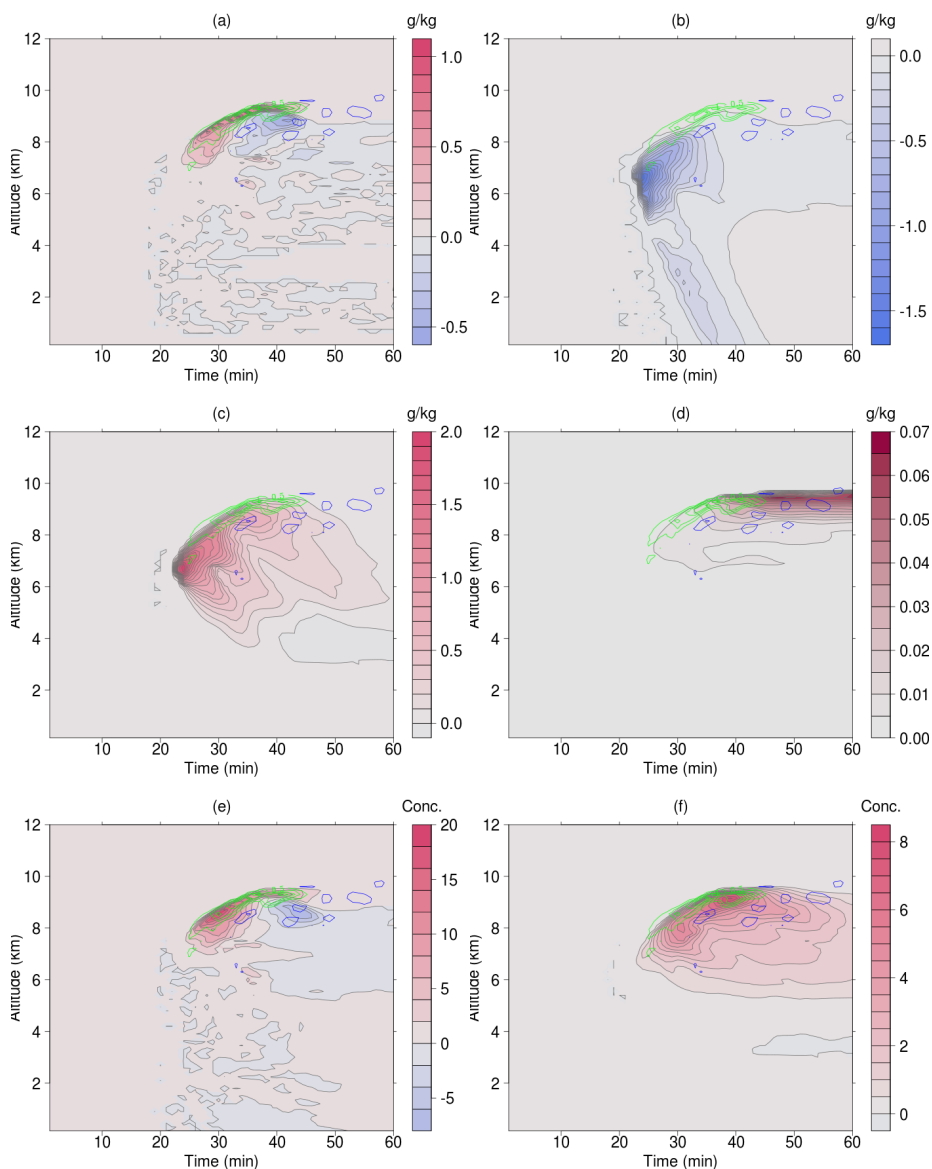
Figure 7. Difference between the sensitivity run, RLX10, and the control run, CTL: (a) cloud water mixing ratio ($\mathrm{gkg^{-1}}$), (b) rain water mixing ration ($\mathrm{gkg^{-1}}$), (c) graupel mixing ratio ($\mathrm{gkg^{-1}}$), (d) ice mixing ration ($\mathrm{gkg^{-1}}$), (e) raindrop concentration (per litre), and (f) graupel concentration (per litre), respectively. Imposed on are the difference in vertical velocity, with green lines indicating
625 **positive and blue lines negative, and the intervals being 0.5 ms^{-1}.**
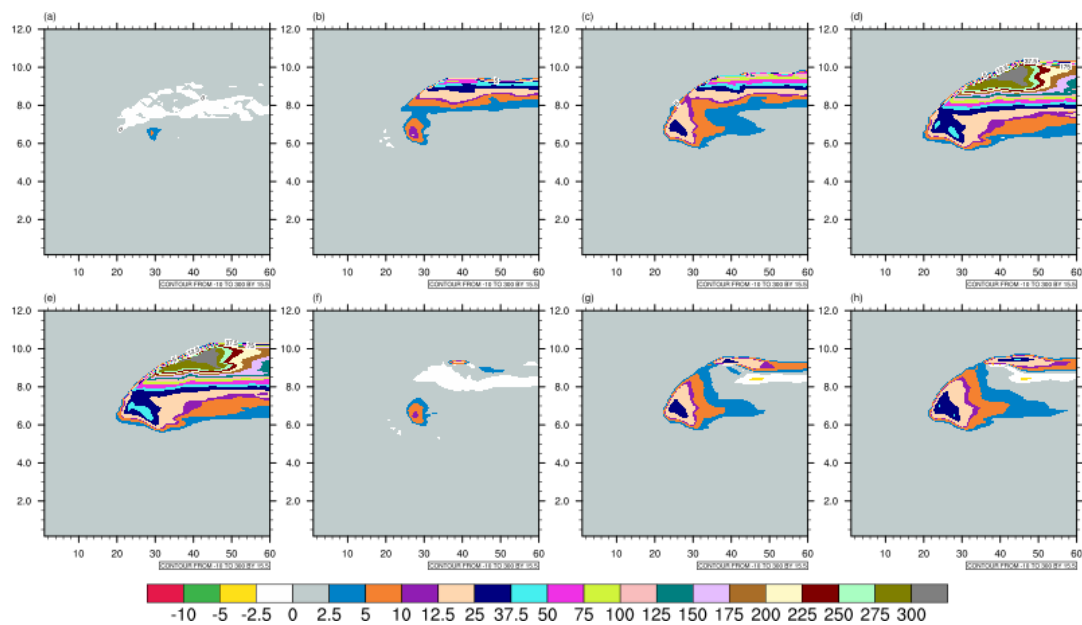
Figure 8. Difference in the ice crystal concentrations (per litre) between sensitivity run and the CTL run: (a) RLX, (b) TEN, (c) RLX10, (d) RLX3X100, (e) RLX2X100, (f) DMTA, (g) DMLRLX, and (h) DLTRLX2, respectively. The x-axis and y-axis are time (min) and altitude (km), respectively.

630
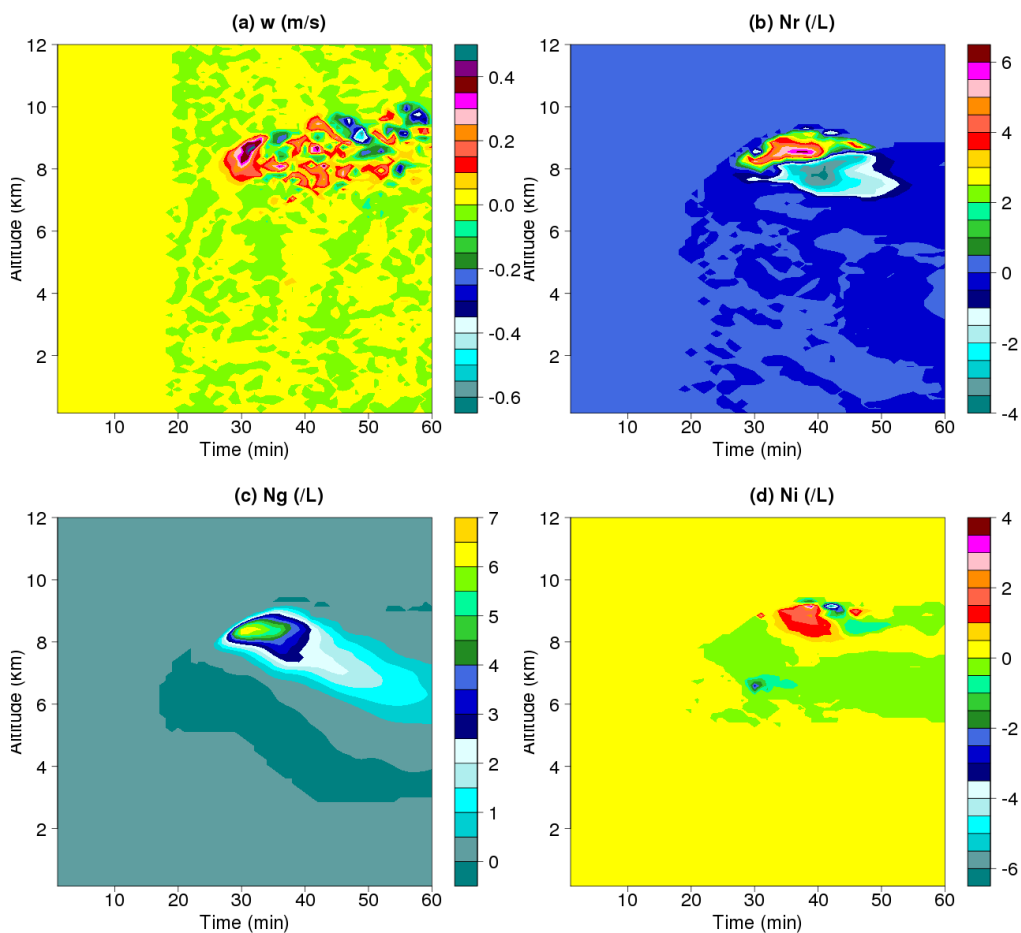
635 **Figure 9. Difference between the PAUKERT run and the CTL run: (a) vertical velocity (ms⁻¹), (b) raindrop number concentration (per litre), (c) the graupel concentrations (per litre), and (d) the ice crystal concentrations (per litre), respectively.**
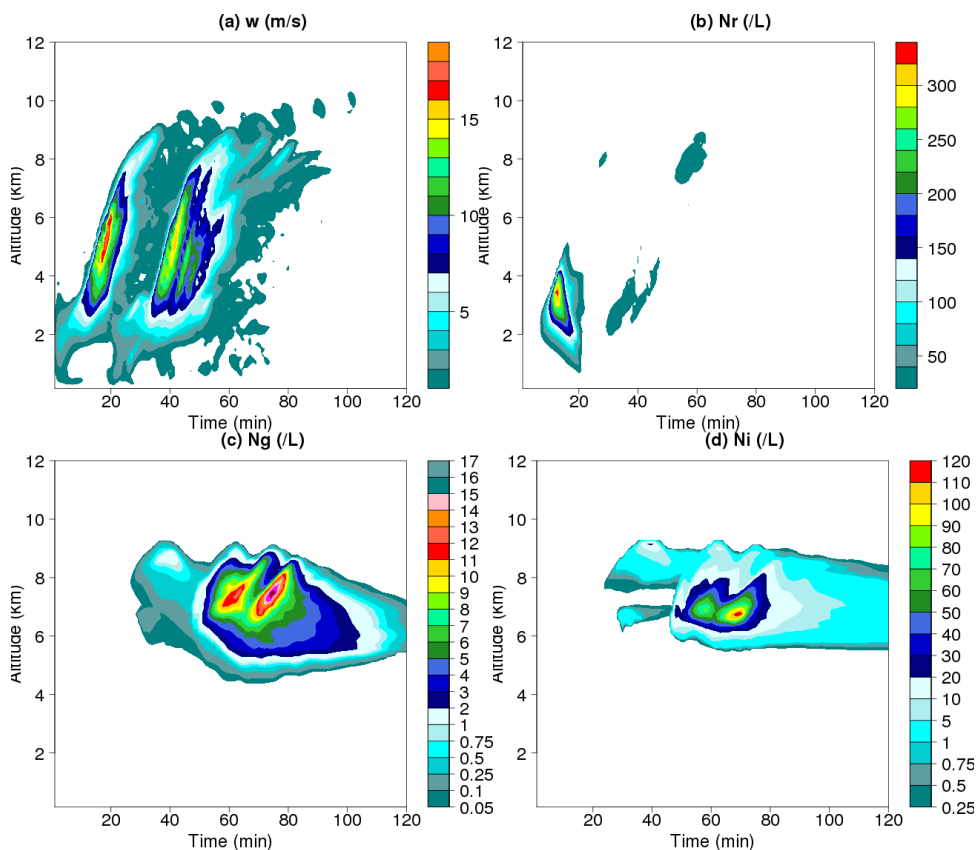
Figure 10. Time-height variations of maximum values in vertical velocity (a), raindrop concentration (b), graupel particle concentration (c), and ice crystal concentration (d) in the two thermal run (THERMALS).
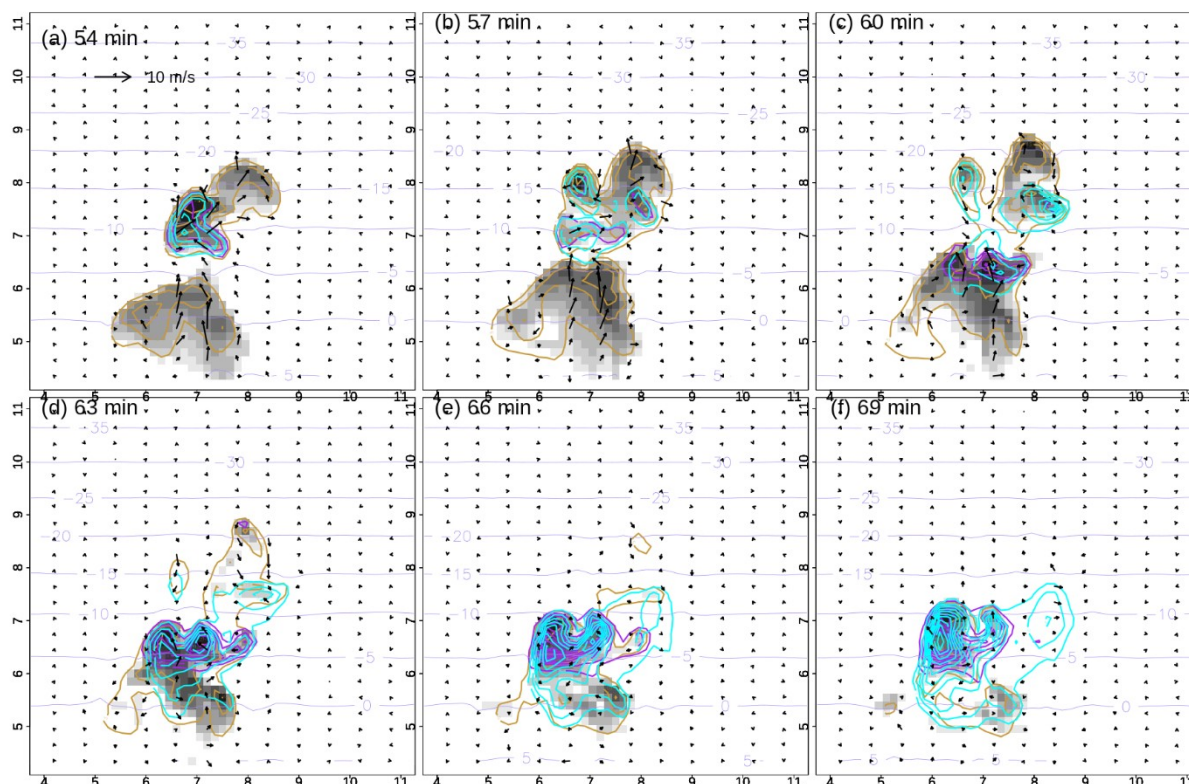
Figure 11. Time sequence for the THERMAL run of spatial distribution of wind vectors, concentration of raindrops, ice crystals, and graupel particles at (a) 54 min, (b) 57 min, (c) 60 min, (d) 63 min, (e) 66 min and (f) 69 min. The orange, pupple and cyan lines are the concentration of raindrops (intervals at $2L^{-1}$), ice crystals (intervals at $10L^{-1}$), and graupel particles (intervals at $2L^{-1}$), respectively. Cloud drop mass mixing ratio is shown in shade in each panel. The cyan lines are isotherms in ∘C. The maximum concentrations are shown in each panel in L^{-1}. The scale for the wind vectors is also shown in (a).

650
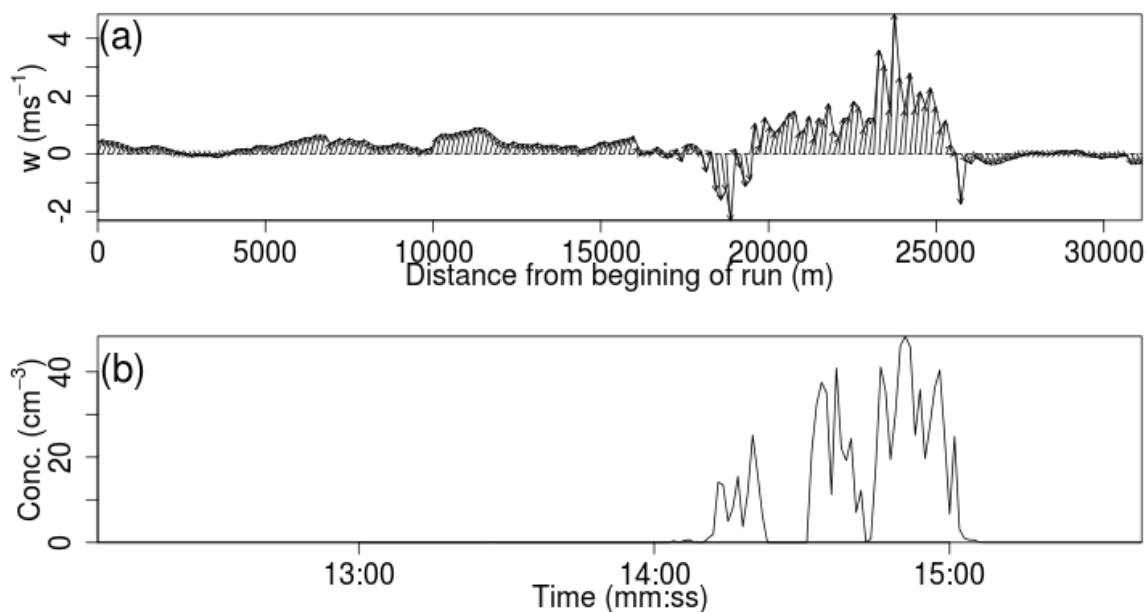
Figure 12. Variations of the vector winds (a) and cloud drop concentration measured with the CDP (b).

655
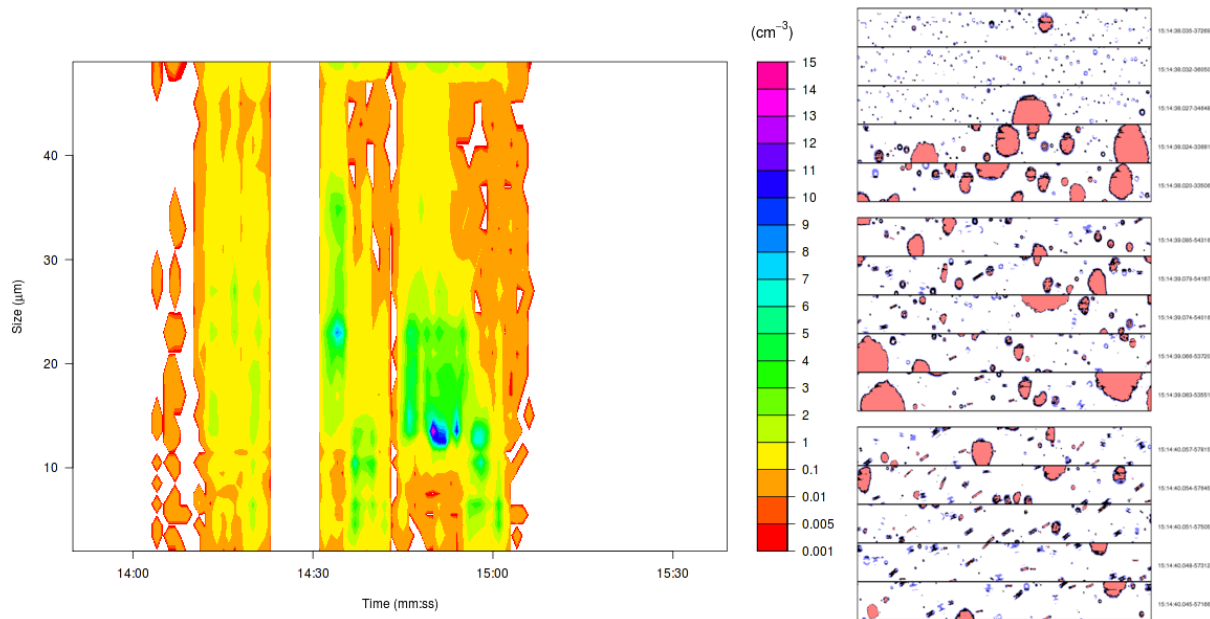
Figure 13. (left): Size distribution of drops measured with the Cloud Drop Probe, and (right) examples of images measured with the Cloud Imaging Probes during Run 6.